Role of helicity in triad interactions in three-dimensional turbulence investigated by a new shell model

Nicholas M. Rathmann[*] and Peter D. Ditlevsen[†]

Niels Bohr Institute, University of Copenhagen, 1017 Copenhagen K, Denmark

Fully developed homogeneous isotropic turbulence in two dimensions is fundamentally different from that in three dimensions. In two dimensions, the simultaneous inviscid conservation of both kinetic energy and enstrophy within the inertial range of scales leads to a forward cascade of enstrophy and a reverse cascade of energy. In three dimensions, helicity, the integral of the scalar product of velocity and vorticity, is also an inviscid flow invariant along with the energy. Unlike the enstrophy, however, the helicity does not block the forward cascade of energy to small scales. Energy and helicity are conserved not only globally but also within each nonlinear triadic interaction between three plane waves in the spectral form of the Navier-Stokes equation (NSE). By decomposing each plane wave into two helical modes of opposite helicities, each triadic interaction is split into a set of eight helical triadic interactions between helical modes [F. Waleffe, Phys. Fluids A **4**, 350 (1992)]. Recently it was found that a subset of these helical interactions, which render both signs of helicity separately conserved (enstrophy-like), leads to an inverse cascade of (part of) the energy [L. Biferale *et al.*, Phys. Rev. Lett. **108**, 164501 (2012)]. Motivated by this finding we introduce a new shell model, obtained from the NSE expressed in the helical basis, allowing the eight helical interactions to be coupled as in the NSE and their relative contributions evaluated as a function of both the net helicity input and triad geometry. By numerically integrating the new model, we find that the intermittency of the energy cascade decreases with the net helicity input. Studying the partitioning of the energy cascade between the eight helical interactions, we find that the decrease in intermittency is related to a shift in the dominating helical interactions when helically forced, two of which exhibit a larger cascade intermittency than the other six interactions. Among the relatively local triad geometries considered here, the partitioning of the energy and helicity cascades between the eight helical interactions shows no sign of change with triad geometry.

I. INTRODUCTION

The role played by helicity in the cascade processes of fully developed three-dimensional (3D) turbulence is elusive. Helicity, the integral of the scalar product of vorticity and velocity, is an inviscid invariant thought to be more or less passively advected through the energy cascade from the large integral scale to the small viscous (dissipating) Kolmogorov scale of the flow. This stands in contrast to two-dimensional (2D) turbulence, where the enstrophy, the integral of the vorticity squared, is a second positive inviscid invariant besides energy. The ratio of the dissipation of enstrophy to the dissipation of energy scales with the Kolmogorov scale η as η^{-2}, thus for $\eta \to 0$ the forward cascade of enstrophy prevents a forward cascade of energy, which instead is transported to larger scales. Following Waleffe [1] we refer to this as a reverse cascade, synonymous to an inverse or upscale cascade.

A similar scaling argument for 3D turbulence leads to the ratio of dissipation of helicity to dissipation of energy scaling as η^{-1}. Thus for a constant dissipation of helicity the dissipation of energy vanishes when $\eta \to 0$. Unlike the 2D case, however, this does not prevent a forward cascade of energy because helicity is not sign specific, implying that the separate dissipation of positive and negative helicity structures can grow as η^{-1}, while the net dissipation of both energy and helicity balance their respective inputs at the forcing scale. In recent work by Biferale *et al.* [2] it was proposed that

if only interactions between same-signed helicity modes are considered, a phenomenon corresponding to the reverse energy cascade in 2D turbulence could be present in the 3D case, with sign-fixed helicity playing the role of enstrophy.

In the spectral representation of the Navier-Stokes equation (NSE), nonlinear interactions are represented by exchanges of energy and helicity between three plane waves under the constraint that their wave vectors (momenta) sum to 0, thereby forming triangles (triads). In the interest of investigating the role played by helicity in an incompressible flow, it is useful to further decompose the spectral velocity components $\mathbf{u}(\mathbf{k})$ in terms of helical modes. Under the helical decomposition spectral velocity components $\mathbf{u}(\mathbf{k})$ are decomposed onto a plane perpendicular to $\mathbf{k}$ using the incompressibility $\mathbf{k} \cdot \mathbf{u}(\mathbf{k}) = 0$ such that $\mathbf{u}(\mathbf{k}) = u_+(\mathbf{k})\mathbf{h}_+(\mathbf{k}) + u_-(\mathbf{k})\mathbf{h}_-(\mathbf{k})$. The basis vectors $\mathbf{h}_\pm(\mathbf{k})$ are eigenvectors of the curl operator, i.e., $i\mathbf{k} \times \mathbf{h}_\pm(\mathbf{k}) = \pm k\mathbf{h}_\pm(\mathbf{k})$, leading to the energy and helicity being given by

$$E = \sum_{\mathbf{k}} (|u_+(\mathbf{k})|^2 + |u_-(\mathbf{k})|^2), \tag{1}$$

$$H = \sum_{\mathbf{k}} k(|u_+(\mathbf{k})|^2 - |u_-(\mathbf{k})|^2) \tag{2}$$

and the spectral form of the NSE being given by [1]

$$(\partial_t + \nu k^2)u_s(\mathbf{k}) = -1/4 \sum_{\mathbf{k}+\mathbf{k}'+\mathbf{k}''=0} \sum_{s',s''} (s'k' - s''k'')$$

$$\mathbf{h}_{s'}^*(\mathbf{k}') \times \mathbf{h}_{s''}^*(\mathbf{k}'') \cdot \mathbf{h}_s^*(\mathbf{k}) \, u_{s'}^*(\mathbf{k}')u_{s''}^*(\mathbf{k}''), \tag{3}$$

where $\{s,s',s''\} = \pm 1$ are helical signs. The inner sum indicates that each triadic interaction is split into a set of $2^3 = 8$

_____

[*]rathmann@nbi.ku.dk

[†]pditlev@nbi.ku.dk

distinct helical triadic interactions, or *subinteractions*, among the helical modes. The interaction coefficient

$$(s'k' - s''k'')\mathbf{h}_{s'}^*(\mathbf{k}') \times \mathbf{h}_{s''}^*(\mathbf{k}'') \cdot \mathbf{h}_s^*(\mathbf{k}) \tag{4}$$

will, for a given triad of waves $\mathbf{k} + \mathbf{k}' + \mathbf{k}'' = 0$, give the relative weights of the different subinteractions. By sorting the subinteractions, four pairs with similar interaction coefficients arise [1], $\{s,s',s''\} = \pm\{+,-,+\}$, $\pm\{+,-,-\}$, $\pm\{+,+,-\}$, $\pm\{+,+,+\}$, hereafter referred to as the four types of subinteractions instead of the eight distinct.

By isolating terms in (3) involving only the three wave vectors $\{\mathbf{k},\mathbf{k}',\mathbf{k}''\}$ (a single triad), one finds

$$\partial_t u_s(\mathbf{k}) = (s'k' - s''k'')\, g\, u_{s'}^*(\mathbf{k}')u_{s''}^*(\mathbf{k}''),$$
$$\partial_t u_{s'}(\mathbf{k}') = (s''k'' - sk)\, g\, u_{s''}^*(\mathbf{k}'')u_s^*(\mathbf{k}), \tag{5}$$
$$\partial_t u_{s''}(\mathbf{k}'') = (sk - s'k')\, g\, u_s^*(\mathbf{k})u_{s'}^*(\mathbf{k}'),$$

where $g = -1/4\, \mathbf{h}_{s'}^*(\mathbf{k}') \times \mathbf{h}_{s''}^*(\mathbf{k}'') \cdot \mathbf{h}_s^*(\mathbf{k})$. Multiplying by $u_s^*(\mathbf{k})$, $u_{s'}^*(\mathbf{k}')$, and $u_{s''}^*(\mathbf{k}'')$, respectively, in the three equations, (5), it immediately follows that energy is conserved within each triad since $\partial_t(|u_s(\mathbf{k})|^2 + |u_{s'}(\mathbf{k}')|^2 + |u_{s''}(\mathbf{k}'')|^2) = 0$, and similarly for the helicity since $\partial_t(sk|u_s(\mathbf{k})|^2 + s'k'|u_{s'}(\mathbf{k}')|^2 + s''k''|u_{s''}(\mathbf{k}'')|^2) = 0$. Nonlinear fluxes of energy and helicity thus result as the sum of exchanges of these quantities between the three triad legs. Furthermore, by considering the generalized energy- and helicity-like quantities

$$E^{(\alpha)} = \sum_{\mathbf{k}} k^\alpha(|u_+(\mathbf{k})|^2 + |u_-(\mathbf{k})|^2), \tag{6}$$

$$H^{(\beta)} = \sum_{\mathbf{k}} k^\beta(|u_+(\mathbf{k})|^2 - |u_-(\mathbf{k})|^2), \tag{7}$$

it is straightforward to show that such quantities are similarly conserved within each triad if the exponents α and β fulfill

$$(s'k'/k - s''k''/k) + (k'/k)^\alpha(s''k''/k - s)$$
$$+ (k''/k)^\alpha(s - s'k'/k) = 0 \tag{8}$$

and

$$s(s'k'/k - s''k''/k) + s'(k'/k)^\beta(s''k''/k - s)$$
$$+ s''(k''/k)^\beta(s - s'k'/k) = 0, \tag{9}$$

respectively. The quantities $E^{(\alpha)}$ and $H^{(\beta)}$, hereafter referred to as the *pseudoenergy* and *pseudohelicity*, clearly depend on both the specific triad shape by $\{k,k',k''\}$ and the subinteraction by $\{s,s',s''\}$, whereas the proper energy ($\alpha = 0$) and helicity ($\beta = 1$) are globally conserved across all triadic interactions, as they should be.

Given the triad dynamics governed by (5), the linear stability of the fixed points $\{u_s(\mathbf{k}),u_{s'}(\mathbf{k}'),u_{s''}(\mathbf{k}'')\} = \{U_0,0,0\},\{0,U_0,0\},\{0,0,U_0\}$ may easily be calculated. Waleffe [1] proposed that the average energy transfer directions between triad legs might be determined by the stability of these fixed points such that energy flows out of the unstable mode (leg) and into the other two. By this rationale, the above four subinteractions may be divided into two classes (each class consisting of two subinteractions): one class in which energy flows from the smallest wave mode (large scales) into the two larger wave modes (smaller scales), termed the "forward" class, and one class in which the energy flows out of the middle

mode and into the largest and smallest modes, termed the "reverse" class. Here the subinteractions between same-signed helical modes corresponding to the 2D turbulence case are of the reverse class. Note that the largest wave mode (smallest scale) is never an unstable mode.

In fully developed 3D turbulence it is not clear to what extent linear stability analysis is relevant or, more importantly, to what extent mixing of the four subinteractions is essential for the overall behavior of the flow. Even if the flow by some strong symmetry constraints could be prepared in a maximally helical state (of only one helical sign), linear instability would make energy flow into modes of opposite sign, obeying the helicity conservation by creating equal amounts of helicity of both signs in the process. In this work we thus seek to investigate numerically the relative importance of the four subinteractions in a coupled context—in particular, quantifying their relative contributions to the energy and helicity cascades and the energy cascade intermittency as a function of the net helicity input and triad shape. Motivated by this we introduce a new helical shell model inspired by (3) allowing the four subinteractions to be coupled as in the NSE.

Helically decomposed shell models derived from the regular GOY [3] and Sabra [4,5] shell models have already been studied [6–10]. Applying the helical decomposition to these regular models four possible helical shell models may be constructed, each one corresponding to one of the four subinteractions. So far, however, only uncoupled configurations of these four separate helical shell models have been considered [6–10].

Our new model is advantageous over previous helical shell models because:

(1) It is structurally closer to the helically decomposed NSE, (3), by being obtained directly from it.

(2) It contains the coupling strengths equivalent to (4) for the four types of subinteractions (which are naturally derived from the NSE), unlike previous models, for which there currently exists no rationale for coupling the subinteractions.

Similarly to previous helical shell models our new model also consists of four separate models, each one corresponding to one of the four subinteractions among helical modes. In the following we therefore refer to these as the four *submodels* of the new shell model.

In summary the purpose of this work is (a) to introduce the new model (Sec. II), (b) to numerically investigate the roles played by the four submodels (subinteractions) in a coupled configuration as a function of the triad geometry and helicity input (Sec. III), and (c) to compare the new uncoupled submodels with previous studies of (uncoupled) helical shell models, in particular, the helical Sabra model, which is structurally closest to the new model (Sec. IV).

II. THE NEW SHELL MODEL

The new model (source freely available at https://github.com/nicholasmr/rdshellmodel) is obtained from the helically decomposed NSE, (3), in Appendix A by defining complex velocity components $u_n^s \equiv u_s(k_n)\,(s = \pm)$ on an exponentially thinned set of wave-vector magnitudes $k_n = k_0\lambda^n$ for $n = 0,1,\ldots,N$. Within this discretized wave space triadic interactions are permitted only between waves fulfilling the triangle

(a) Submodel 1: $\{s,s',s''\} = \pm\{+,-,+\}$

(b) Submodel 2: $\{s,s',s''\} = \pm\{+,-,-\}$

(c) Submodel 3: $\{s,s',s''\} = \pm\{+,+,-\}$

(d) Submodel 4: $\{s,s',s''\} = \pm\{+,+,+\}$
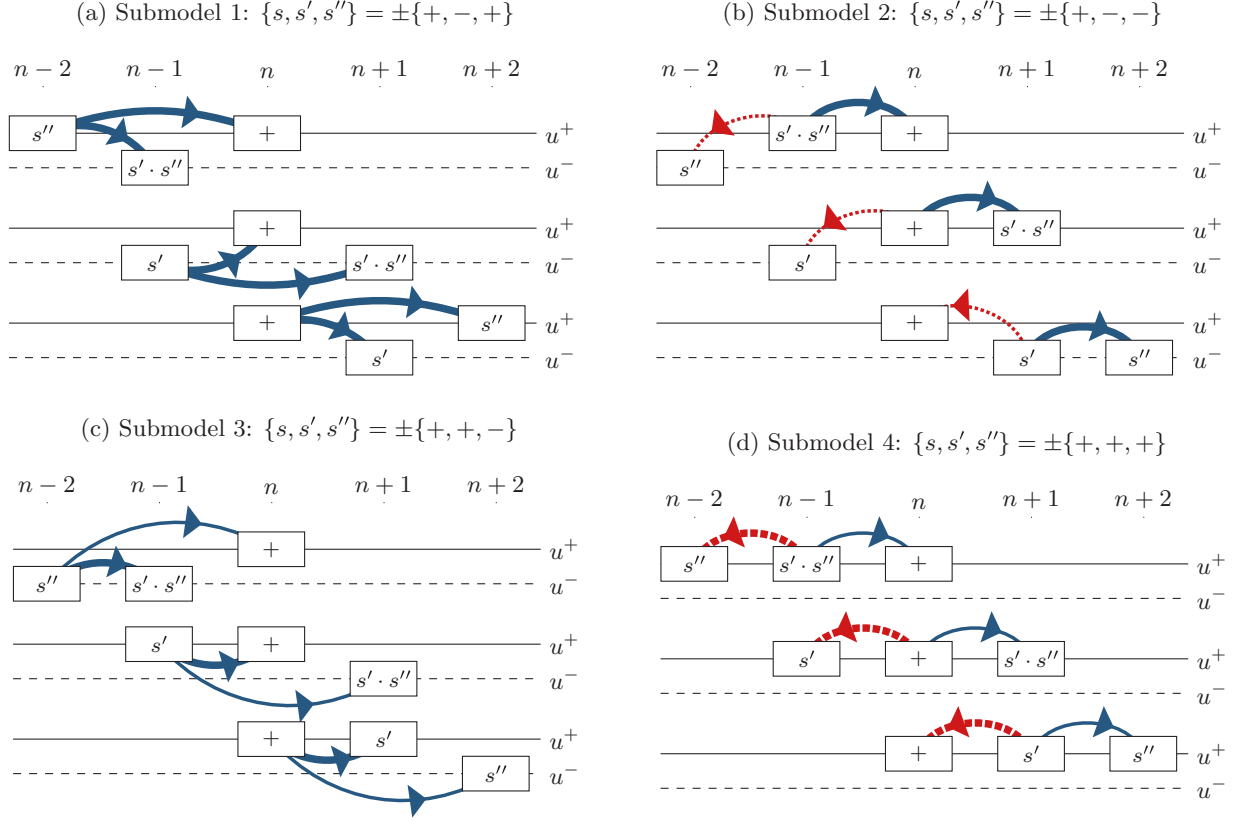
FIG. 1. Schematic of the three nonlinear helical interactions of each submodel coupling to u_n^+. All interactions are sign flipped for complementary interactions coupling to u_n^- (not shown). Arrows indicate the average energy transfer direction within each triadic interaction resulting from a linear stability analysis [1,10]: solid blue (dashed red) arrows denote forward (reverse) energy transfers, while thick (thin) arrows represent dominant (subordinate) transfers.

inequality $k_n + k_{n+p} \geqslant k_{n+q}$ (the shell model equivalent of the NSE constraint $\mathbf{k} + \mathbf{k}' + \mathbf{k}'' = 0$) and $0 < p < q$ [a model constraint ensuring that waves do not self-interact (unilateral triangles) such that Liouville's theorem is fulfilled as for the inviscid part of the NSE].

In the limit of nearest-neighbor interactions the new model is

$$(d_t + D_n)u_n^s = sk_n \sum_{s',s''} g^{s',s''}\left(u_{n+1}^{s \cdot s',*}u_{n+2}^{s \cdot s''} - \frac{\epsilon^{s',s''}}{\lambda}u_{n-1}^{s \cdot s',*}u_{n+1}^{s \cdot s' \cdot s''}\right.$$
$$\left. + \frac{\xi^{s',s''}}{\lambda^2}u_{n-2}^{s \cdot s''}u_{n-1}^{s \cdot s' \cdot s''}\right) + f_n^s, \qquad (10)$$

where λ, k_0, and N are free model parameters and $u_n^{s,*}$ is the complex conjugate of u_n^s. The helical signs of the interacting modes depend on the specific submodel, here written compactly by introducing effective signs built on products of s, s', and s'', e.g., $s \cdot s'$. Forcing and viscous dissipation at the nth shell (scale k_n) of helical sign s are f_n^s and $(\nu k_n^2 + \nu_L k_n^{-4})u_n^s \equiv D_n u_n^s$, respectively, $\nu_L k_n^{-4}u_n^s$ being a large-scale drag added to remove any potential buildup of energy at large scales. The small- and large-scale viscosities ν and ν_L are free parameters, whereas the large-scale drag exponent (-4) was chosen such that the large-scale dissipation is confined to the first few shells for the longest possible inertial range. The specific values of ν_L and the large-scale

drag exponent were found not to influence the model behavior (not shown). The summation over $\{s',s''\}$ is the weighted sum over the four submodels. The four possible pairs $\{s',s''\} = \{-,+\}, \{-,-\}, \{+,-\}, \{+,+\}$ hereafter denote submodels 1–4, respectively, in accordance with previous literature. Thus, three helical triadic interactions are resolved per shell per submodel (Fig. 1).

The submodel weights $g^{s',s''}$ and modal interaction coefficients $\epsilon^{s',s''}$ and $\xi^{s',s''}$ are given by (derived in Appendix A)

$$g^{s',s''}(\lambda) = -s's''(1 + s'\lambda - s''\lambda^2)(s'\lambda - s''\lambda^2), \qquad (11)$$

$$\epsilon^{s',s''}(\lambda) = \frac{1 - s''\lambda^2}{\lambda - s's''\lambda^2}, \qquad (12)$$

$$\xi^{s',s''}(\lambda) = -s''(1 - s'\epsilon^{s',s''}). \qquad (13)$$

The interaction coefficients $g^{s',s''}$, $\epsilon^{s',s''}$, and $\xi^{s',s''}$ depend on the shell model spacing parameter λ which indicates the geometry of the resolved triads: for $\lambda \to 1$ triangles become equilateral (leg lengths $\{1,1,1\}$ relative to the smallest leg), while for $\lambda \to (1 + \sqrt{5})/2 = \varphi$ (golden ratio) they collapse to a line (leg lengths $\{1,\varphi,\varphi^2\}$ relative to the smallest leg). Note that unless triads are closed ($\lambda \leqslant \varphi$), as the NSE requires, the interaction coefficients are not well defined (Appendix B).

Waleffe [1] hypothesized two classes of helical triadic interactions based on the average energy transfer directions
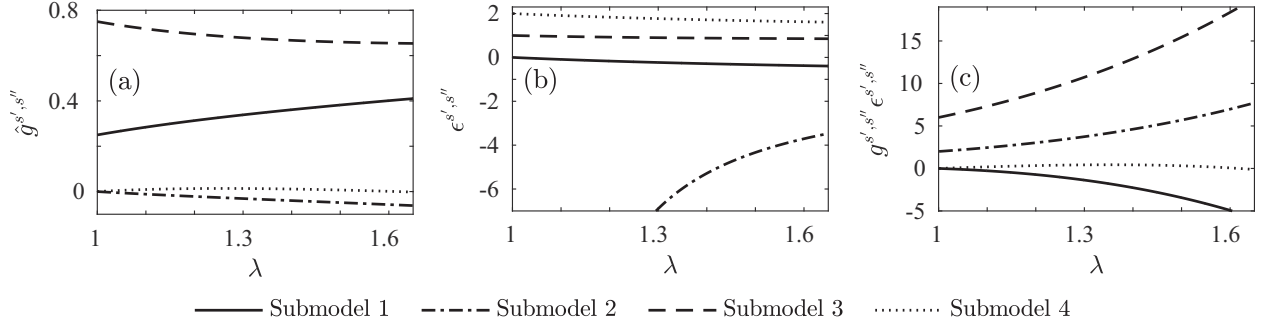
FIG. 2. Submodel (a) coupling strength $g^{s',s''}$, (b) interaction coefficient $\epsilon^{s',s''}$, and (c) their product as a function of λ.

using linear stability: (i) a class of forward interactions (F class) consisting of triads with opposite helical signs of the two largest wave modes and (ii) a class of reverse interactions (R class) consisting of triads with equal helical signs of the two largest wave modes. Thus, two of the four subinteractions belong to the F class, while the remaining two belong to the R class. The R-class interactions for which all three signs are not equal, however, were suggested by Waleffe [1], based on the above instability assumption and a scaling assumption, to become F class for local triadic interactions, defined as the ratio of the smallest to the middle wave number being higher than 0.278. Considering closed-triad nearest-neighbor interactions in the shell model thus renders these interactions purely F class since the ratio is bounded by $1/\lambda \geqslant 1/\varphi = 0.618$.

Because the product of helical signs between the two largest modes in all nonlinear terms of (10) is $s' \cdot s''$, each submodel consists only of interactions of one class. Like the helically decomposed GOY and Sabra models the new model therefore also consists of two submodels of the F class [$s' \cdot s'' = -1$; Figs. 1(a) and 1(c)] and two of the R class [$s' \cdot s'' = +1$; Figs. 1(b) and 1(d)], of which submodel 2 ($\{s',s''\} = \{-,-\}$) contains the dual F- and R-class nature described above.

The interaction coefficients $g^{s',s''}$ and $\epsilon^{s',s''}$ are both plotted as functions of λ in Fig. 2. Figure 2(a) shows the normalized submodel weights $\hat{g}^{s',s''} = g^{s',s''} / \sum_{s',s''} g^{s',s''}$. Since two of the submodels belong to the F class their associated weights ($g^{+,-}$ and $g^{-,+}$) are expected to be the largest because 3D turbulence exhibits an average forward-dominated energy cascade. This is indeed found to be the case. The modal interaction coefficients $\epsilon^{s',s''}$ plotted in Fig. 2(b) indicate that both $s' \cdot s'' = -1$ (F-class) submodels have $|\epsilon^{s',s''}| < 1$, whereas both $s' \cdot s'' = +1$ (R-class) submodels have $|\epsilon^{s',s''}| > 1$. This is appealing because the structure of the new model, (10), and functional forms of $\epsilon^{s',s''}$, (12), resemble, but are not identical to, the helically decomposed GOY and Sabra counterparts. In the GOY and Sabra models it is well known that the limit $\epsilon^{s',s''} = 1$ marks the transition between 2D behavior of the energy cascade ($1 < \epsilon^{s',s''} < 2$) and 3D behavior ($\epsilon^{s',s''} < 1$). The values of $\epsilon^{s',s''}$ thus seem to support the expected F- and R-class behavior based on the $s' \cdot s''$ product.

Invariants and fluxes

Similarly to other shell models the nonlinear terms in (10) conserve both the energy $E = \sum_{n=0}^{N}(|u_n^+|^2 + |u_n^-|^2)$ and the helicity $H = \sum_{n=0}^{N} k_n(|u_n^+|^2 - |u_n^-|^2)$. Additionally,

in the limit of nearest-neighbor interactions each submodel conserves one pseudoenergy quantity $E^{(\alpha)} = \sum_{n=0}^{N} k_n^\alpha(|u_n^+|^2 + |u_n^-|^2)$ and one pseudohelicity quantity $H^{(\beta)} = \sum_{n=0}^{N} k_n^\beta(|u_n^+|^2 - |u_n^-|^2)$, where the exponents α and β are, respectively, constrained by

$$1 - s'\lambda^\alpha \epsilon^{s',s''} + s''(\lambda^\alpha)^2 \xi^{s',s''} = 0, \qquad (14)$$

$$1 - \lambda^\beta \epsilon^{s',s''} + (\lambda^\beta)^2 \xi^{s',s''} = 0, \qquad (15)$$

which are constraints similar to (8) and (9) of the NSE (see Appendix C). These pseudoinvariants are therefore specific to each submodel ($\{s',s''\}$ pair) and the resolved triad shape by λ.

The existence of globally conserved (across all triad interactions) pseudoinvariants within each submodel can potentially influence the behavior of that submodel. However, because pseudoinvariants are not shared among submodels (or triad shapes), only the energy and helicity are globally conserved when mixing submodels (or triad shapes), similarly to the NSE (Appendix C).

Nonlinear spectral fluxes of energy and helicity through the nth shell are given as the transfers from all wave numbers less than k_n to wave numbers larger than k_n, that is, $\Pi_n^E = d_t \sum_{m=0}^{n}(|u_m^+|^2 + |u_m^-|^2)$ and $\Pi_n^H = d_t \sum_{m=0}^{n} k_m (|u_m^+|^2 - |u_m^-|^2)$. Following the calculations through the yields for a single submodel (see Appendix D)

$$\Pi_n^E = \Delta_{n+1}^{-,s',s''} + (1 - s'\epsilon^{s',s''})\Delta_n^{-,s',s''}, \qquad (16)$$

$$\Pi_n^H = k_n\left(\Delta_{n+1}^{+,s',s''} + (\lambda^{-1} - \epsilon^{s',s''})\Delta_n^{+,s',s''}\right), \qquad (17)$$

where the correlators are defined as

$$\Delta_n^{\pm,s',s''} = 2k_{n-1} \operatorname{Re}\left[u_{n-1}^{+,*} u_n^{s',*} u_{n+1}^{s''} \pm u_{n-1}^{-,*} u_n^{-s',*} u_{n+1}^{-s''}\right]. \qquad (18)$$

For the coupled model the corresponding expressions are merely the weighted sums of (16) and (17) using weights $g^{s',s''}$.

III. NUMERICAL RESULTS: 1. THE COUPLED MODEL

The coupling strengths, (11) [Fig. 2(a)], suggest that the influence of F-class interactions (submodels 1 and 3) should dominate over that of R-class interactions (submodels 2 and 4) in a coupled configuration. However, due to the strong nonlinearities present in (10) the relative influence of the four submodels might not be so simple and might possibly depend on the triad shape and net helicity input. In this work we are therefore interested in quantifying the relative
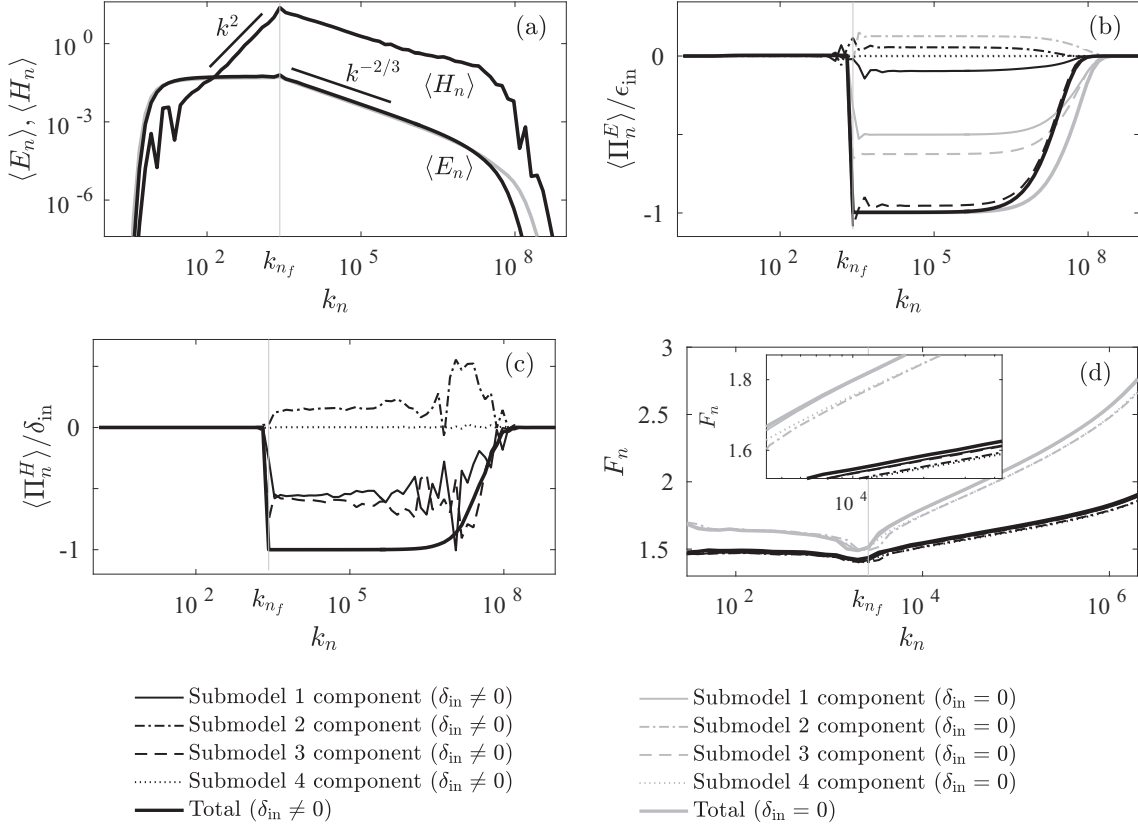
FIG. 3. Simulated coupled model (a) energy and helicity spectra and (b, c) energy and helicity fluxes. Also shown are (b, c) the individual submodel contributions of the energy and helicity cascades and (d) the energy cascade intermittency. Black lines denote the helically forced scenario ($\delta_{\rm in} \neq 0$), whereas gray lines denote the nonhelically forced scenario ($\delta_{\rm in} = 0$).

contributions from the four individual submodels to the energy and helicity cascades and the energy cascade intermittency as a function of the helicity input and triad shape. To do so we considered multiple triad shapes (λ values) along with two forcing scenarios: (i) a maximally helical forcing (of only one sign) and (ii) nonhelical forcing (of both signs). Since numerical results were found not to depend on the triad shape λ (discussed below), here, for the sake of brevity, we present the results of just one configuration—$\lambda = 1.3$, $k_0 = 1$, $N = 81$, $\nu = 10^{-11}$, and $\nu_L = 10^3$—implying the coupling strengths $\{\hat{g}^{-,+}, \hat{g}^{-,-}, \hat{g}^{+,-}, \hat{g}^{+,+}\} = \{0.34, -0.03, 0.68, 0.01\}$ and $\epsilon^{s',s''}$ values $\{\epsilon^{-,+}, \epsilon^{-,-}, \epsilon^{+,-}, \epsilon^{+,+}\} = \{-0.23, -6.89, 0.89, 1.76\}$. The value $\lambda = 1.3$ was chosen for conformity with a future planned study considering coupled non-nearest-neighbor interactions ($\lambda = 1.3$ allows a total of seven triad geometries; see Appendixes A and B for details). The values chosen for k_0 and N were found not to influence the model behavior (not shown). The number of shells N determines the highest resolved wave number and is limited by hardware capabilities (integration time) due to the stiffness of the system. Because the large- and small-scale viscosities ν and ν_L affect only the length of the inertial ranges, and not their dynamics (not shown), their values were chosen such that dissipation occurs at the ends of the resolved wave space for the longest possible inertial ranges. A fourth-order Runge-Kutta integration scheme was applied in all simulations using $dt = 5 \times 10^{-8}$ together with the forcing $f_{n_f}^{\pm} = (1 + i)/u_{n_f}^{\pm,*}$ applied to shell $n_f = 30$, supplying a constant input of energy $\epsilon_{\rm in}$ (not to be confused with the

interaction coefficient $\epsilon^{s',s''}$) and helicity $\delta_{\rm in}$. The choice of forcing scale was found not to influence the results (not shown). Two forcing scenarios were employed: one in which only the positive 30th helical shell is forced such that $\epsilon_{\rm in} = 2$, hereafter referred to as the $\delta_{\rm in} \neq 0$ (helical) simulations (where $\delta_{\rm in} = k_{30}\epsilon_{\rm in}$); and one in which both 30th helical shells are forced such that $\epsilon_{\rm in} = 4$, hereafter referred to as the $\delta_{\rm in} = 0$ (nonhelical) simulations. All realizations are 10^{11} time steps long and were initialized using the velocity profile $u_n^{\pm} \sim k_n^{-1/3}$. A spin-up of 10^{10} time steps was performed to eliminate transients from the statistics, which was determined by the plateauing of the total energy content and the shell 1 and 20 energy content.

Figure 3(a) shows the coupled model simulated energy and helicity spectra for both the helically ($\delta_{\rm in} \neq 0$) and the nonhelically ($\delta_{\rm in} = 0$) forced case. Under both forcing scenarios the energy spectrum scales K41-like as $\langle E_n \rangle \sim k_n^{-2/3}$ for wave numbers $k_n > k_{n_f}$, associated with a forward energy cascade [Fig. 3(b)]. For wave numbers $k_n < k_{n_f}$ (large scales) the energy is found to equilibrate. The seemingly small positive $\langle E_n \rangle$ scaling for $k_n < k_{n_f}$ is due to an insufficiently short spectral range connecting the forcing scale with the large-scale sink, which is evident from equivalent simulations using a smaller forcing scale (not shown). The helicity spectrum is found to scale linearly with the energy spectrum for $k_n > k_{n_f}$ [Fig. 3(a)], i.e., $\langle E_n \rangle \sim \langle H_n \rangle \sim k_n^{-2/3}$, associated with a forward helicity cascade [Fig. 3(c)]. This behavior

matches expectations for the dual forward energy and helicity cascades envisaged by Brissaud *et al.* [11]. For the large scales $k_n < k_{n_f}$ the helicity spectrum matches its equilibrium spectrum $\langle H_n \rangle \sim k_n^2$ based on the equipartitioning of the energy and helicity (same method as presented in Sec. IV below; not shown).

Figures 3(b) and 3(c) additionally show how the total $\langle \Pi_n^E \rangle$ and $\langle \Pi_n^H \rangle$ fluxes are partitioned among the four submodels, calculated by (16) and (17) multiplied by the weights $g^{s',s''}$. Figure 3(b) shows the forward energy cascade in nonhelical turbulence (gray lines) is predominantly carried by submodel 1 and 3 interactions, whereas submodels 2 and 4 both contribute with relatively small up-scale cascades, the former being more than an order of magnitude larger than the latter. In helical turbulence, however, the forward energy cascade is carried almost entirely by submodel 3 interactions (black lines), whereas the forward helicity cascade is dominated equally by submodel 1 and 3 interactions while submodel 2 contributes a small reverse component [Fig. 3(c)]. In the interest of determining how this partitioning might depend on the triad geometry multiple λ values were additionally considered. The values tested were $\lambda = \{1.1, 1.2, 1.3, 1.4, 1.5, 1.6\}$ together with $N = \{223, 116, 81, 63, 52, 45\}$ and $n_f = \{83, 44, 30, 24, 20, 17\}$, respectively, thus ensuring that k_N and k_{n_f} are approximately unchanged. All interaction coefficients were updated according to (11)–(13) to reflect the different λ values. Across all λ values no change in cascade partitioning was found (not shown), albeit only relatively local triads (similar leg sizes) are possible in the nearest-neighbor interaction limit considered here.

In order to understand how the change in dominant helical interactions with the net helicity input influences the energy cascade intermittency we quantify the intermittency, similarly to De Pietro *et al.* [10], by the shell-energy flatness

$$F_n = S_4(k_n)/(S_2(k_n))^2, \tag{19}$$

where the structure functions $S_q(k_n)$ are defined in terms of Π_n^E by

$$S_q(k_n) = \langle (k_n^{-1}|\Pi_n^E|)^{q/3} \rangle. \tag{20}$$

Figure 3(d) shows the flatness F_n calculated using the total energy flux as well as using the individual submodel contributions to Π_n^E. Interestingly, the energy cascade in helical turbulence is found to be less intermittent than that in nonhelical turbulence. The zoom-in in Fig. 3(d) shows that the flatnesses calculated using the individual submodel contributions to Π_n^E are largest for submodels 1 and 3 under both forcing scenarios.

As an explanation for the change in intermittency one might hypothesize that the different submodels each possess different degrees of cascade intermittency, such as found by De Pietro *et al.* [10], but this is masked in coupled configurations as Fig. 3(d) suggests. If so, one would anticipate the flatness of submodel 1 to be greatest among the four submodels in stand-alone uncoupled simulations. In the follow section we investigate this hypothesis and compare the uncoupled submodels with those in previous studies considering other helical shell models.

IV. NUMERICAL RESULTS: 2. THE UNCOUPLED SUBMODELS

The uncoupled submodels were integrated individually using the same configuration as listed in Sec. III. However, due to the submodel-dependent scaling of inertial ranges, the viscosity ν was chosen separately for each submodel configuration to ensure that dissipation occurs at the end of the resolved wave space for the longest possible inertial ranges. The large-scale viscosity was meanwhile kept fixed at $\nu_L = 10^3$. For each of the four submodels the same two forcing scenarios were applied as in the coupled configuration.

Figures 4(a) and 4(c) show the submodel 1–4 energy fluxes and spectra, respectively, of the nonhelically forced simulations ($\delta_{in} = 0$). The helically forced simulations ($\delta_{in} \neq 0$) display similar results but are not shown in Fig. 4, for clarity. The results show that submodels 1–3 all exhibit the expected K41 scaling $\langle E_n \rangle \sim k_n^{-2/3}$ associated with a forward energy cascade for wave numbers $k_n > k_{n_f}$. For wave numbers $k_n < k_{n_f}$ (large scales) the three submodels have distinctly different spectra. Submodel 4, however, is different from submodels 1–3 in the entire spectrum. This submodel is found to transfer energy upscale but does not exhibit any scaling of the energy spectrum for $k_n < k_{n_f}$. The scaling for wave numbers $k_n > k_{n_f}$ is approximately $\langle E_n \rangle \sim k_n^{-4/3}$, corresponding to a forward cascade of (positive) helicity.

Figures 4(b) and 4(d) show the helicity fluxes and spectra, respectively, of the helically forced simulations ($\delta_{in} \neq 0$). The results show that submodels 2 and 3 both exhibit helicity spectra scaling K41-like as $\langle H_n \rangle \sim k_n^{-2/3}$ for $k_n > k_{n_f}$, which are accompanied by forward cascades of helicity. Submodels 1 and 4 also exhibit downscale cascades of helicity but with spectra scaling as $\langle H_n \rangle \sim k_n \langle E_n \rangle$.

In order to explain the dissimilar submodel behaviors found for $k_n < k_{n_f}$, in the following we differentiate between the parts of the simulated energy spectra in which flow invariants equipartition among shells from those parts in which invariants cascade [12]. Using the equipartition theorem, a conservative system with quadratic invariants, in this case E, $E^{(\alpha)}$, H, and $H^{(\beta)}$, will on average distribute the conserved quantities equally between the degrees of freedom in the system [13]. In the present case the submodel partition function therefore takes the form $Z = \int \exp[-\sum_n ((A + A^{(\alpha)} k_n^\alpha + Bk_n + B^{(\beta)} k_n^\beta)|u_n^+|^2 + (A + A^{(\alpha)} k_n^\alpha - Bk_n - B^{(\beta)} k_n^\beta)|u_n^-|^2)] \Pi_i du_i^+ du_i^-$, where A, $A^{(\alpha)}$, B, and $B^{(\beta)}$ are the inverse E, $E^{(\alpha)}$, H, and $H^{(\beta)}$ temperatures, respectively. Using the partition function the equilibrated energy and helicity spectra are easily calculated, giving

$$\langle E(k_n) \rangle = \frac{A + A^{(\alpha)} k_n^\alpha}{\left(A + A^{(\alpha)} k_n^\alpha\right)^2 - \left(Bk_n + B^{(\beta)} k_n^\beta\right)^2}$$
$$\approx \frac{1}{A + A^{(\alpha)} k_n^\alpha}, \tag{21}$$

$$\langle H(k_n) \rangle = \frac{k_n \left(Bk_n + B^{(\beta)} k_n^\beta\right)}{\left(A + A^{(\alpha)} k_n^\alpha\right)^2 - \left(Bk_n + B^{(\beta)} k_n^\beta\right)^2}$$
$$\approx \frac{k_n \left(Bk_n + B^{(\beta)} k_n^\beta\right)}{\left(A + A^{(\alpha)} k_n^\alpha\right)^2}, \tag{22}$$
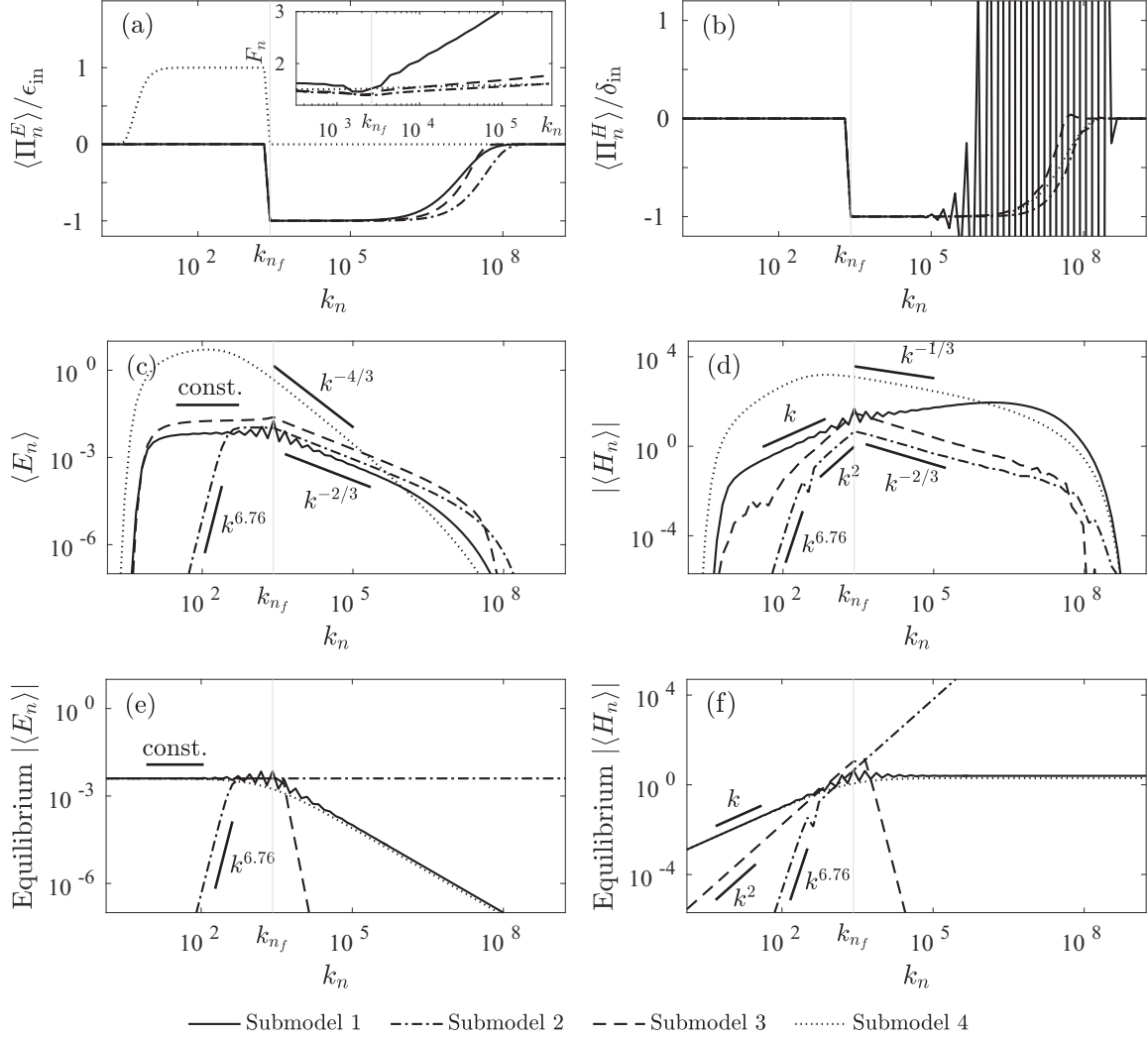
FIG. 4. Simulated uncoupled submodel (a, b) energy and helicity fluxes and (c, d) energy and helicity spectra. (a) The corresponding calculated flatnesses using (19). (e, f) Equilibrium spectra predicted by (21) and (22).

where $(A + A^{(\alpha)}k_n^\alpha)^2 \gg (Bk_n + B^{(\beta)}k_n^\beta)^2$ has been used for the approximate forms by noting that the energy spectra of the helical ($\delta_{\text{in}} \neq 0$) and nonhelical ($\delta_{\text{in}} = 0$) simulations are similar (not shown). The inverse temperatures may be constrained by equating the average dissipation of the four invariants to their average inputs $\epsilon_{\text{in}}, \delta_{\text{in}} = k_{n_f}\epsilon_{\text{in}}, \epsilon_{\text{in}}^{(\alpha)} = k_{n_f}^\alpha \epsilon_{\text{in}}$, and $\delta_{\text{in}}^{(\beta)} = k_{n_f}^\beta \epsilon_{\text{in}}$, where n_f is the forcing shell. Of course, the actual dissipation is the integrated effect over a large range of scales. However, in order to obtain useful expressions for the temperatures we approximate these as one effective (Kolmogorov) scale per quantity, hereafter denoted $k_E, k_{E^{(\alpha)}}, k_H$ and $k_{H^{(\beta)}}$. Equating input to dissipation then gives the approximate

expressions

$$\epsilon_{\text{in}} \approx D(k_E)\langle E(k_E)\rangle, \tag{23}$$

$$\delta_{\text{in}} \approx D(k_H)\langle H(k_H)\rangle, \tag{24}$$

$$\epsilon_{\text{in}}^{(\alpha)} \approx D(k_{E^{(\alpha)}})k_{E^{(\alpha)}}^\alpha \langle E(k_{E^{(\alpha)}})\rangle, \tag{25}$$

$$\delta_{\text{in}}^{(\beta)} \approx D(k_{H^{(\beta)}})k_{H^{(\beta)}}^{\beta-1}\langle H(k_{H^{(\beta)}})\rangle, \tag{26}$$

where $D(k_n) = \nu k_n^2 + \nu_L k_n^{-4}$, $\langle E^{(\alpha)}(k_n)\rangle = k_n^\alpha \langle E(k_n)\rangle$, and $\langle H^{(\beta)}(k_n)\rangle = k_n^{\beta-1}\langle H(k_n)\rangle$. Combining the above expressions all temperatures are related to A by

$$\frac{A^{(\alpha)}}{A} = \frac{D(k_E)k_{E^{(\alpha)}}^{-\alpha} - D(k_{E^{(\alpha)}})k_{n_f}^{-\alpha}}{D(k_{E^{(\alpha)}})k_{n_f}^{-\alpha}k_{E^{(\alpha)}}^\alpha - D(k_E)}, \tag{27}$$

$$\frac{B^{(\beta)}}{B} = \frac{\left(1 + k_{H^{(\beta)}}^\alpha \frac{A^{(\alpha)}}{A}\right)D(k_H)k_{n_f}^{\beta-1}k_H^2 - \left(1 + k_H^\alpha \frac{A^{(\alpha)}}{A}\right)D(k_{H^{(\beta)}})k_{H^{(\beta)}}^{\beta+1}}{\left(1 + k_H^\alpha \frac{A^{(\alpha)}}{A}\right)D(k_{H^{(\beta)}})k_{H^{(\beta)}}^{2\beta} - \left(1 + k_{H^{(\beta)}}^\alpha \frac{A^{(\alpha)}}{A}\right)D(k_H)k_{n_f}^{\beta-1}k_H^{\beta+1}}, \tag{28}$$

$$\frac{B}{A} = \frac{D(k_E)k_{n_f}\left(1 + k_H^\alpha \frac{A^{(\alpha)}}{A}\right)^2}{D(k_H)k_H\left(1 + k_E^\alpha \frac{A^{(\alpha)}}{A}\right)\left(k_H + k_H^\beta \frac{B^{(\beta)}}{B}\right)}. \tag{29}$$

TABLE I. Approximate dissipation scales used in (27)–(29) for best fits of (21) and (22) with the simulated energy and helicity spectra in Figs. 4(c) and 4(d).

Submodel	k_E	$k_{E^{(\alpha)}}$	k_H	$k_{H^{(\beta)}}$
1	4.2×10^3	2.5×10^3	2.5×10^3	4.2×10^3
2	1.0×10^4	5.0×10^2	4.5×10^3	4.1×10^2
3	4.2×10^3	3.0×10^3	5.5×10^3	4.0×10^3
4	5.0×10^1	6.5×10^4	6.5×10^4	5.0×10^1

Inserting (27)–(29) into (21) and (22), Figs. 4(e) and 4(f) show the submodel equilibrium spectra with $A = 1 \times 10^3$ [for offsets comparable to Figs. 4(c) and 4(d)] and $n_f = 30$ (as in simulations) using the dissipation scales listed in Table I obtained from best fits to the simulated spectra in Figs. 4(c) and 4(d) and corresponding pseudoinvariant spectra (not shown).

Comparing the simulated spectra $\langle E_n \rangle$ and $\langle H_n \rangle$ of submodels 1–3 with the equilibrium spectra, one finds that they agree well, suggesting equipartitioning of the energy (E_n) and pseudoenergy ($k_n^\alpha E_n$) for $k_n < k_{n_f}$. As in the coupled model case the weak positive scaling of $\langle E_n \rangle$ simulated by submodels 1 and 3 is due to an insufficiently short spectral range connecting the forcing scale with the large-scale sink, which is evident from equivalent simulations using a smaller forcing scale (not shown). The simulated $\langle H_n \rangle$ spectra of submodels 1–3 also match the expected equilibrium spectra in Fig. 4(f) for $k_n < k_{n_f}$, which remarkably even captures the small dip exhibited by submodel 2.

Before moving on to submodel 4 let us consider the scaling behavior for wave numbers $k_n > k_{n_f}$ of submodels 1–3. In this spectral range energy fluxes are constant, which is fulfilled if the correlators scale as $\Delta_n^{-,s',s''} \sim$ const., implying velocity components scaling as $u_n^{\pm} \sim k_n^{-1/3}$. One would thus expect $\langle E_n \rangle \sim k_n^{-2/3}$, which is indeed found to be the case. The energy and helicity fluxes indicate dual downscale (forward) cascades of both quantities in submodels 1–3 [Figs. 4(a) and 4(b)]. Brissaud *et al.* [11] envisaged that such dual downscale cascades would manifest themselves by the helicity spectrum scaling linearly with the energy spectrum, i.e., $\langle E_n \rangle \sim \langle H_n \rangle \sim k_n^{-2/3}$, which is here indeed found to be the case [Fig. 4(d)], similarly to the coupled model [Fig. 3(a)].

The energy and helicity spectra of submodel 4 do not resemble their equilibrium spectra, suggesting that equipartitioning of flow invariants is not responsible for the shapes of the spectra. Following the above K41 scaling argument one might expect the energy spectrum to scale as $\sim k_n^{-2/3}$ for $k_n < k_{n_f}$ due to the energy cascade and as $\sim k_n^{-4/3}$ for $k_n > k_{n_f}$ due to the helicity cascade (by a similar argument), but this is clearly not the case for $k_n < k_{n_f}$. The failure of the K41 argument may be understood from the specific ratios $\langle \Pi_n^E \rangle / \langle \Pi_n^H \rangle$ in the two inertial ranges of the flow which allow the correlators to be scale dependent while simultaneously supporting constant energy and helicity fluxes. In submodel 4 helical modes of opposite signs do not interact, thus if there is no pumping of a specific sign of helicity, all modes of that sign will decay. In this case the correlators reduce to $\Delta_n^{+,+,+} = \Delta_n^{-,+,+} = 2k_{n-1} \text{Re}[u_{n-1}^{+,*} u_n^{+,*} u_{n+1}^{+}] \equiv \Delta_n^{\star}$. Calculating the ratio $\langle \Pi_n^E \rangle / \langle \Pi_n^H \rangle$ by inserting $\Delta_n^{\star}$ into (16) and
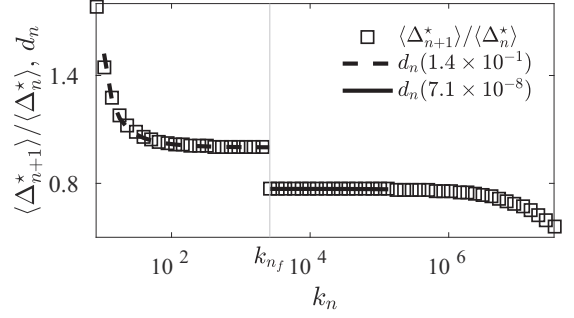
FIG. 5. Simulated submodel 4 correlator ratios (squares) and predicted ratios based on (30) (solid and dashed lines).

(17), one finds the exact relation

$$\frac{\langle \Delta_{n+1}^{\star} \rangle}{\langle \Delta_n^{\star} \rangle} = \frac{\epsilon^{+,+} - k_n \langle \Pi_n^E \rangle / \langle \Pi_n^H \rangle - 1}{1 - k_n \langle \Pi_n^E \rangle / \langle \Pi_n^H \rangle} \equiv d_n \big(\langle \Pi_n^E \rangle / \langle \Pi_n^H \rangle \big),$$

(30)

which may be scale sensitive depending on $\langle \Pi_n^E \rangle / \langle \Pi_n^H \rangle$. The simulated ratios are found to be $\langle \Pi_n^E \rangle / \langle \Pi_n^H \rangle = 1.4 \times 10^{-1}$ in the inertial range $k_n < k_{n_f}$ (shell 10–28 average) and $\langle \Pi_n^E \rangle / \langle \Pi_n^H \rangle = 7.1 \times 10^{-8}$ in the intertial range $k_n > k_{n_f}$ (shell 32–45 average). Using these ratios Fig. 5 shows the simulated $\langle \Delta_{n+1}^{\star} \rangle / \langle \Delta_n^{\star} \rangle$ values compared to the anticipated d_n forms, plotted only in their valid ranges where fluxes are constant. The correlators clearly exhibit scale dependence for $k_n < k_{n_f}$ following d_n, thus suggesting that the K41 argument leading to $\langle E_n \rangle \sim k_n^{-2/3}$ is not necessarily valid.

The new shell model introduced here is obtained from the helical decomposition of the NSE. It is remarkable that the three helical interactions per shell of each submodel are similar to those of the helically decomposed GOY and Sabra submodels apart from the interaction coefficients [6–10]. Benzi *et al.* [7] implemented the four helical submodels in a GOY model. Interestingly, the (absolute) values of $\epsilon^{s',s''}$ indicate that the new model, similarly to the GOY model, consists of two submodels (1 and 4) with canonical 2D and 3D $\epsilon^{s',s''}$ configurations and one new 3D type (Sec. II). The last submodel (submodel 2) was found by Benzi *et al.* [7] to show signs of a reverse energy cascade, a property not shared by the new model in its nearest-neighbor limit (multiple free parameter combinations were tested as specified below; not shown).

Recent work by De Pietro *et al.* [10] also numerically investigated the Sabra model equivalent of submodel 2, finding the energy spectrum scaling as $\langle E_n \rangle \sim k_n^{-0.28}$ for wave numbers $k_n < k_{n_f}$, as opposed to the energy/pseudoenergy equipartitioning found here. In order to test the possible influence of the choice of free parameters on the scaling properties of the new submodel 2 multiple parameter combinations were considered: $\lambda = \{1.3, 1.4, 1.5\}$, $k_0 = \{0.5, 1, 4\}$, $N = \{81, 63, 52\}$, $n_f = \{30, 40, 50\}$, and $\nu_L = \{10^1, 10^2, 10^3\}$ (with different large-scale drag exponents: $-2, -4$). All these configurations, which each properly closes triads as required by the NSE ($\lambda \leqslant \varphi$), were found to behave similarly to the above results (not shown). If, on the other hand, the shell spacing λ exceeds the golden ratio φ (open triads), we find scaling behavior matching that found by De Pietro
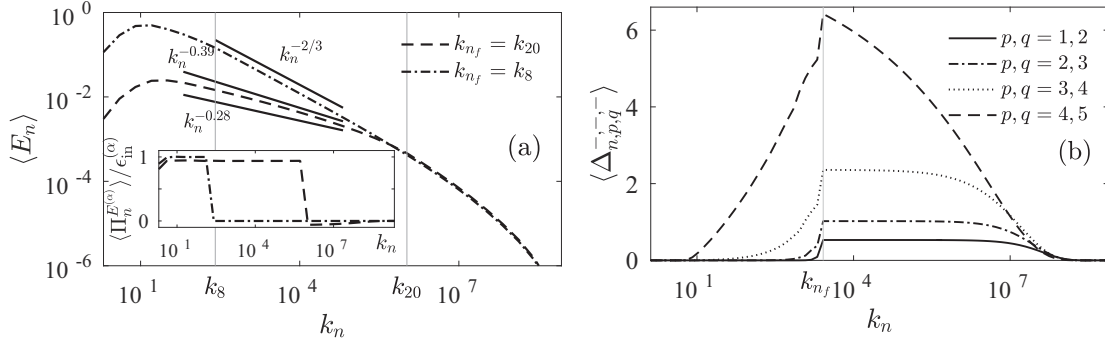
FIG. 6. (a) Simulated energy spectra of submodel 2 when configured as by De Pietro *et al.* [10] ($\lambda = 2$ with $k_{n_f} = k_8$ or $k_{n_f} = k_{20}$) and (b) simulated energy correlators of submodel 2 ranging from nearest-neighbor $\{p,q\} = \{1,2\}$ (local) interactions to non-nearest-neighbor (nonlocal) interactions. Panel (a) additionally shows the existence of a reverse psuedoenergy cascade (normalized by the mean pseudoenergy input $\epsilon_{\text{in}}^{(\alpha)} = k_{n_f}^\alpha \epsilon_{\text{in}}$).

et al. [10]. Figure 6(a) shows the simulated energy spectrum of submodel 2 configured approximately as by De Pietro *et al.* [10], with $\lambda = 2$, $N = 31$, $\nu_L = 1$, and $\nu = 10^{-12}$, forced either at shell $n_f = 8$ or at shell $n_f = 20$ using a helical forcing (a nonhelical forcing produces similar results; not shown). Here, however, we suggest that the scaling $\langle E_n \rangle \sim k_n^{2\alpha/3} = k_n^{-0.39}$ for $k_n < k_{n_f}$ arising from the reverse cascade of psuedoenergy [Fig. 6(a)] is a better fit compared to $\langle E_n \rangle \sim k_n^{-0.28}$ based on a suggested zero-mode solution [10]. Note that the pseudoinvariants are shared between the two models since the interaction coefficients are related by $\epsilon_{(\text{Sabra})}^{s',s''} = s' \epsilon^{s',s''}$ and $\xi_{(\text{Sabra})}^{s',s''} = -s'' \xi^{s',s''}$, leading to the same conservation constraint, (14), for the Sabra model.

Similarly to De Pietro *et al.* [10] we also find the flatnesses among the uncoupled submodels to be largest in submodel 1 for $k_n > k_{n_f}$, although they did not consider submodel 3.

Finally, De Pietro *et al.* [10] found that the direction of the energy cascade in a Sabra-type submodel 2 depends on triad shape as suggested by Waleffe [1]. By extending the interaction scope to interactions between shells $\{n,n+p,n+q\}$ for $0 < p < q$ ($\{p,q\} = \{1,2\}$ being the nearest-neighbor limit considered above), nonlocal triads (smallest-to-middle wave-number ratio <0.278) may be constructed, allowing the predicted F- to R-class transition to be investigated. Doing so, they explained the cascade transition by noting the time-averaged energy correlators of submodel 2, $\langle \Delta_{n,p,q}^{-,s',s''} \rangle = \langle \Delta_{n,p,q}^{-,-,-} \rangle$, are asymptotically constant (independent of n) within inertial ranges. If so, the time-averaged non-nearest-neighbor equivalent of (16) (see Appendix D) becomes $\langle \Pi_n^E \rangle = ((q - 1) + (q - p - 1)\epsilon_{p,q}^{-,-}) \langle \Delta_{n,p,q}^{-,-,-} \rangle \equiv F_{p,q} \langle \Delta_{n,p,q}^{-,-,-} \rangle$, and the sign of $F_{p,q}$ determines the cascade direction as a function of the triad shape (determined by $\{\lambda,p,q\}$) since the sign of $\langle \Delta_{n,p,q}^{-,-,-} \rangle$ may be determined from a linear stability analysis and is shape independent. However, because of the dissimilar correlator definitions between the Sabra model and the new model, the energy correlators of the new model might behave differently. In order to test this three additional simulations were carried out for the non-nearest-neighbor interactions $\{p,q\} = \{2,3\},\{3,4\},\{4,5\}$ (implying $\epsilon_{p,q}^{-,-} = \{-6.31,-5.85,-5.50\}$, respectively) using configurations otherwise similar to the submodel 2 setup described in Sec. IV (details on the non-nearest-neighbor interaction models is presented in Ap-

pendixes A–D). The simulated correlators are shown in Fig. 6(b) and are found to exhibit scale dependence with decreased interaction locality (large p,q), suggesting that some other explanation is needed for the reversal of the energy cascade in the nonlocal triad limit (not shown). This will be the focus of a subsequent study considering in detail the role played by pseudoinvariants, which will be published elsewhere.

Gilbert *et al.* [14] showed that a regular Sabra model in the 2D configuration $\epsilon^{+,+} > 1$, corresponding to submodel 4 here, exhibits different $\langle E_n \rangle$ scaling regimes depending on the value of $\epsilon^{+,+}$. Their works suggests that whenever $\epsilon^{+,+}/\lambda < 1 + \lambda^{-2/3}$ the reverse energy flux regime should be accompanied by a proper K41 scaling energy spectrum, whereas above this critical value a quasiequilibrium energy spectrum should develop. Inserting $\epsilon^{+,+}$ from (12) one would thus always expect a K41 scaling to occur. However, present simulations can hardly be said to scale as $\langle E_n \rangle \sim k_n^{-2/3}$ or to be in quasiequilibrium for $k_n < k_{n_f}$. In order to further compare submodel 4 with their work, additional simulations were therefore conducted using $\lambda = \{1.1,1.2,1.3,1.4,1.5,1.6,2.0\}$ with $N = \{146,76,53,41,37,34,22\}$, respectively (ensuring k_N are approximately the same). In all cases energy spectra were found to behave as in Fig. 4(c) (not shown), suggesting that the work by Gilbert *et al.* [14] does not carry over to submodel 4 of the new model.

V. SUMMARY

The role of helicity in 3D turbulence was numerically investigated in the context of a new shell model obtained as a special case of the helically decomposed Navier-Stokes equation (NSE) [1]. Unlike previous shell models, the new model can couple the four naturally occurring subsets of helical triadic interactions (subinteractions) similarly to the NSE, thereby allowing their individual roles to be investigated in a coupled context. By considering forcing scenarios with and without an input of helicity we find that the (forward) energy cascade in helical turbulence is less intermittent than that in nonhelical turbulence for local triadic interactions. The energy cascade in helical turbulence was found to be carried almost entirely by subinteractions of the third type,

whereas in nonhelical turbulence the cascade is partitioned roughly equally between subinteraction 1 and subinteraction 3. This large influence exerted by subinteractions 1 and 3 matches expectations based on real 3D turbulence, in which these subinteractions are thought to exclusively contribute to a forward energy cascade [1]. Additionally, by varying the resolved triad shape we find no change in simulated behavior or cascade partitioning, albeit only relatively local triads (similar leg sizes) are possible in the nearest-neighbor interaction limit considered here.

In order to understand the decreased intermittency arising from a net helicity input the four individual subinteractions (submodels) were simulated separately (uncoupled) in the limit of local triadic interactions, which share several similarities with the four existing helically decomposed Sabra shell models. These simulations showed that the cascade intermittency of submodel 1 far exceeds the other three, thus explaining the decreased intermittency in helical turbulence where subinteraction type 1 is suppressed when coupled with the other three.

In accordance with expectations three of the four submodels (submodels 1–3) contribute with dual downscale (forward) cascades of energy and helicity, whereas the last submodel (submodel 4), which renders both signs of helicity separately inviscidly conserved (enstrophy-like), transfers energy upscale and helicity downscale.

In the coupled model and the three dual-cascading submodels (submodels 1–3) flow invariants were found to equipartition in the range of scales $k_n < k_{n_f}$ (k_{n_f} being the forcing scale), which was explained using the equipartition theorem with multiple conserved quadratic quantities. The remaining submodel 4, however, exhibits a reverse energy cascade for $k_n < k_{n_f}$ but has a very small weight in comparison to the other submodels in the full set of triadic interactions of the helically decomposed dynamics. By investigating the scaling behavior of the triple correlations used in energy and helicity flux calculations of submodel 4, it was found these cannot

necessarily be assumed to be scale independent within inertial ranges. If so, as was found to be the case numerically, this prevents the traditional shell model K41-style argument from being used, otherwise leading to an anticipated $\langle E(k_n) \rangle \sim k_n^{-2/3}$ scaling energy spectrum within energy cascade regimes.

APPENDIX A: THE NEW SHELL MODEL

In order to obtain the new model from the helically decomposed Navier-Stokes equation (NSE), (3), it is necessary to impose two constraints: (i) spectral velocity components are assumed to be independent of direction in **k** space, $u_s(\mathbf{k}) = u_s(k\hat{\mathbf{k}}) = u_s(k)$, and (ii) reducing **k** space to include only components which are increasingly spaced in magnitude according to the geometrical progression $k_n = k_0 \lambda^n$ for $n = 0, 1, \ldots, N$. Within this wave set, only cross-scale triadic interactions are considered, i.e., triads in which all three wave components have different magnitudes, which is inspired by the structure of the GOY and Sabra shell models. Since only cross-magnitude interactions are considered, it is useful to split the triadic sum in the NSE, (3), into three separate sums, hereafter referred to as the three triad *groups*, for which **k** is the smallest ($k < k' < k''$), middle ($k' < k < k''$), and largest ($k' < k'' < k$) wave number. Note that double-primed vectors are chosen to be larger than single-primed ones, which leads to no loss of generality due to symmetry when interchanging the dummy waves $\mathbf{k}' \leftrightarrow \mathbf{k}''$ (and $s' \leftrightarrow s''$). Additionally, the vectorial condition $\mathbf{k} + \mathbf{k}' + \mathbf{k}'' = 0$ on each triadic sum can be rewritten by expressing the largest mode as the sum of the two smaller and absorbing the resulting negative signs into the terms of the sums using reality $\mathbf{u}(-\mathbf{k}) = \mathbf{u}^*(\mathbf{k})$ and the basis property $\mathbf{h}_s(-\mathbf{k}) = \mathbf{h}_{-s}(\mathbf{k})$ [1]. The vectorial condition on each triadic sum thus becomes $\mathbf{k} + \mathbf{k}' = \mathbf{k}''$, $\mathbf{k} + \mathbf{k}' = \mathbf{k}''$, and $\mathbf{k} = \mathbf{k}' + \mathbf{k}''$ for groups 1, 2, and 3, respectively, and the NSE, (3), then takes the form

$$
\begin{aligned}
(\partial_t + \nu k^2) u_s(\mathbf{k}) = -\frac{1}{4} \sum_{s',s''} \Bigg[&\sum_{\substack{\mathbf{k}+\mathbf{k}'=\mathbf{k}'' \\ k<k'<k''}} (s'k' - s''k'') \mathbf{h}_{s'}^*(\mathbf{k}') \times \mathbf{h}_{-s''}^*(\mathbf{k}'') \cdot \mathbf{h}_s^*(\mathbf{k}) u_{s'}^*(\mathbf{k}') u_{s''}(\mathbf{k}'') \\
&- \sum_{\substack{\mathbf{k}+\mathbf{k}'=\mathbf{k}'' \\ k'<k<k''}} (s'k' - s''k'') \mathbf{h}_s^*(\mathbf{k}) \times \mathbf{h}_{-s''}^*(\mathbf{k}'') \cdot \mathbf{h}_{s'}^*(\mathbf{k}') u_{s'}^*(\mathbf{k}') u_{s''}(\mathbf{k}'') \\
&+ \sum_{\substack{\mathbf{k}=\mathbf{k}'+\mathbf{k}'' \\ k'<k''<k}} (s'k' - s''k'') \mathbf{h}_{-s''}^*(\mathbf{k}'') \times \mathbf{h}_s^*(\mathbf{k}) \cdot \mathbf{h}_{-s'}^*(\mathbf{k}') u_{s'}(\mathbf{k}') u_{s''}(\mathbf{k}'') \Bigg]
\end{aligned}
\tag{A1}
$$

where the antisymmetric property of $\mathbf{h}_{s'}^*(\mathbf{k}') \times \mathbf{h}_{s''}^*(\mathbf{k}'') \cdot \mathbf{h}_s^*(\mathbf{k})$ has been used to rearrange the order of basis components in a way which shall be useful later.

In the interest of dropping the direction dependencies $\hat{\mathbf{k}}$, $\hat{\mathbf{k}}'$, and $\hat{\mathbf{k}}''$, consider further splitting the three triadic sums in (A1) into sums over triad shapes and triad orientations,

respectively,

$$\sum_{\substack{\mathbf{k}+\mathbf{k}'=\mathbf{k}'' \\ k<k'<k''}} = \sum_{\substack{k',k'' \\ k+k' \geqslant k'' \\ k<k'<k''}} \sum_{\substack{\hat{\mathbf{k}}',\hat{\mathbf{k}}'' \\ k\hat{\mathbf{k}}+k'\hat{\mathbf{k}}'=k''\hat{\mathbf{k}}''}}, \qquad (A2)$$

$$\sum_{\substack{\mathbf{k}+\mathbf{k}'=\mathbf{k}'' \\ k'<k<k''}} = \sum_{\substack{k',k'' \\ k+k' \geqslant k'' \\ k'<k<k''}} \sum_{\substack{\hat{\mathbf{k}}',\hat{\mathbf{k}}'' \\ k\hat{\mathbf{k}}+k'\hat{\mathbf{k}}'=k''\hat{\mathbf{k}}''}}, \qquad (A3)$$

$$\sum_{\substack{\mathbf{k}=\mathbf{k}'+\mathbf{k}'' \\ k'<k''<k}} = \sum_{\substack{k',k'' \\ k'+k'' \geqslant k \\ k'<k''<k}} \sum_{\substack{\hat{\mathbf{k}}',\hat{\mathbf{k}}'' \\ k\hat{\mathbf{k}}=k'\hat{\mathbf{k}}'+k''\hat{\mathbf{k}}''}}. \qquad (A4)$$

From here, reducing the $\mathbf{k}$ space to include only components with magnitudes given by $k_n = k_0 \lambda^n$ allows the three sums

over triad shapes to be rejoined: Depending on λ, the triangle inequality constrains the possible choices of n in k_n which can be combined to construct triads. Consider therefore the range of integers p and q sorted by $0 < p < q$ which fulfill the triangle inequality $k_n + k_{n+p} \geqslant k_{n+q}$, thereby allowing any triad geometry to be constructed when $\lambda \to 1$ for large or small enough values of $\{p,q\}$. From this reduction it immediately follows that $\{k',k''\} = \{k_{n+p}, k_{n+q}\}$ for the first group, thus turning the sum over $\{k',k''\}$ into a sum over $\{p,q\}$. The corresponding $\{k',k''\}$ sums of groups 2 and 3 may be written in terms of the same $\{p,q\}$ sum as group 1 by noting that the constraints imposed by (A3) and (A4) are, respectively, fulfilled if $\{k',k''\} = \{k_{n-p}, k_{n+q-p}\}$ and $\{k',k''\} = \{k_{n-q}, k_{n+p-q}\}$, which produces triad shapes similar to group 1. Substituting in the above, one finds

$$
\begin{aligned}
\left(\partial_t + \nu k_n^2\right) u_s(k_n \hat{\mathbf{k}}) = -\frac{1}{4} k_n \sum_{\substack{p,q \\ 0<p<q \\ k_n+k_{n+p} \geqslant k_{n+q}}} \sum_{s',s''} \Bigg[& \sum_{\substack{\hat{\mathbf{k}}',\hat{\mathbf{k}}'' \\ k_n\hat{\mathbf{k}}+k_{n+p}\hat{\mathbf{k}}'=k_{n+q}\hat{\mathbf{k}}''}} (s'\lambda^p - s''\lambda^q) \mathbf{h}_{s'}^*(k_{n+p}\hat{\mathbf{k}}') \times \mathbf{h}_{-s''}^*(k_{n+q}\hat{\mathbf{k}}'') \cdot \mathbf{h}_s^*(k_n\hat{\mathbf{k}}) \, u_{s'}^*(k_{n+p}\hat{\mathbf{k}}') u_{s''}(k_{n+q}\hat{\mathbf{k}}'') \\
& - \sum_{\substack{\hat{\mathbf{k}}',\hat{\mathbf{k}}'' \\ k_n\hat{\mathbf{k}}+k_{n-p}\hat{\mathbf{k}}'=k_{n+q-p}\hat{\mathbf{k}}''}} \frac{s'-s''\lambda^q}{\lambda^p} \mathbf{h}_s^*(k_n\hat{\mathbf{k}}) \times \mathbf{h}_{-s''}^*(k_{n+q-p}\hat{\mathbf{k}}'') \cdot \mathbf{h}_{s'}^*(k_{n-p}\hat{\mathbf{k}}') \, u_{s'}^*(k_{n-p}\hat{\mathbf{k}}') u_{s''}(k_{n+q-p}\hat{\mathbf{k}}'') \\
& + \sum_{\substack{\hat{\mathbf{k}}',\hat{\mathbf{k}}'' \\ k_n\hat{\mathbf{k}}=k_{n-q}\hat{\mathbf{k}}'+k_{n+p-q}\hat{\mathbf{k}}''}} \frac{s'-s''\lambda^p}{\lambda^q} \mathbf{h}_{-s''}^*(k_{n+p-q}\hat{\mathbf{k}}'') \times \mathbf{h}_s^*(k_n\hat{\mathbf{k}}) \cdot \mathbf{h}_{-s'}^*(k_{n-q}\hat{\mathbf{k}}') \, u_{s'}(k_{n-q}\hat{\mathbf{k}}') u_{s''}(k_{n+p-q}\hat{\mathbf{k}}'') \Bigg].
\end{aligned}
$$

$$(A5)$$

Dropping now the direction dependencies $\hat{\mathbf{k}}$, $\hat{\mathbf{k}}'$, and $\hat{\mathbf{k}}''$, the compact shell model notation $u_n^{s,*} = u_s^*(k_n)$ is adopted. Moreover, because only one mode per magnitude is resolved, the inner sums over $\{\hat{\mathbf{k}}',\hat{\mathbf{k}}''\}$ (triad orientation) are also dropped. Having assumed direction independence, the rotational term (complex exponential) in the geometry term is assumed to be discardable, allowing it to be written more compactly as

$$
\begin{aligned}
\mathbf{h}_{s'}^*(\mathbf{k}') &\times \mathbf{h}_{s''}^*(\mathbf{k}'') \cdot \mathbf{h}_s^*(\mathbf{k}) \\
&= -\frac{Q(k,k',k'')}{2kk'k''} ss's''(sk+s'k'+s''k'') \\
&\equiv \Lambda_{s',s'',s}(k',k'',k) = \Lambda_{s',s'',s}(\lambda^p,\lambda^q,1) \equiv \Lambda_{s',s'',s}^{p,q}, \quad (A6)
\end{aligned}
$$

where (i) the group 1 associations $\{k',k''\} = \{k_{n+p}, k_{n+q}\}$ are used in the $\Lambda_{s',s'',s}^{p,q}$ definition (groups 2 and 3 could equally have been used), (ii) the scale-independent property $\Lambda_{s',s'',s}(k_{n+p}, k_{n+q}, k_n) = \Lambda_{s',s'',s}(\lambda^p, \lambda^q, 1)$ has been used (i.e., only relative leg sizes matter), and (iii) $Q(k,k',k'') = (2k^2k'^2 + 2k'^2k''^2 + 2k''^2k^2 - k^4 - k'^4 - k''^4)^{1/2}$ (see Waleffe [1] for details). With this compacted notation Eq. (A5) may then be

written as

$$
\begin{aligned}
\left(d_t + \nu k_n^2\right) u_n^s &\\
= -\frac{1}{4} k_n \sum_{\substack{p,q \\ 0<p<q \\ k_n+k_{n+p} \geqslant k_{n+q}}} \sum_{s',s''} \Bigg[& (s'\lambda^p - s''\lambda^q) \Lambda_{s',-s'',s}^{p,q} u_{n+p}^{s',*} u_{n+q}^{s''} \\
& - \frac{s'-s''\lambda^q}{\lambda^p} \Lambda_{s,-s'',s'}^{p,q} u_{n-p}^{s',*} u_{n+q-p}^{s''} \\
& + \frac{s'-s''\lambda^p}{\lambda^q} \Lambda_{-s'',s,-s'}^{p,q} u_{n-q}^{s'} u_{n+p-q}^{s''} \Bigg]
\end{aligned}
$$

$$(A7)$$

by using the scale-independent property of $\Lambda_{s',s'',s}^{p,q}$, allowing all wave magnitudes in the geometry terms of groups 2 and 3 in (A5) to be multiplied through by λ^p and λ^q, respectively.

This expression is in fact a weighted sum of four helical shell models in disguise. To realize this, one needs to expand the sum over helical signs. Doing so, one finds three terms per $\{s',s''\}$ contribution involving

(i) $\Lambda_{+,-,+}^{p,q}$, $\Lambda_{+,-,+}^{p,q}$, $\Lambda_{-,+,-}^{p,q}$ for $\{s',s''\} = \{+,+\}$,

(ii) $\Lambda_{+,+,+}^{p,q}$, $\Lambda_{+,+,+}^{p,q}$, $\Lambda_{+,+,-}^{p,q}$ for $\{s',s''\} = \{+,-\}$,

(iii) $\Lambda_{-,-,+}^{p,q}$, $\Lambda_{+,-,-}^{p,q}$, $\Lambda_{-,+,+}^{p,q}$ for $\{s',s''\} = \{-,+\}$,

(iv) $\Lambda_{-,+,+}^{p,q}$, $\Lambda_{+,+,-}^{p,q}$, $\Lambda_{+,+,+}^{p,q}$ for $\{s',s''\} = \{-,-\}$.

Collecting terms sharing Λ using the reflection property $\Lambda_{-s',-s'',-s}^{p,q} = \Lambda_{s',s'',s}^{p,q}$ and defining $G_{p,q}(\lambda) = 1/8 \, Q(1,\lambda^p,\lambda^q)/(\lambda^p\lambda^q)$, the new shell model is uncovered,

$$(d_t + D_n)u_n^s = sk_n \sum_{\substack{p,\,q \\ 0<p<q \\ k_n+k_{n+p} \geqslant k_{n+q}}} G_{p,q} \sum_{s',s''} g_{p,q}^{s',s''} \left(u_{n+p}^{s\cdot s',*} u_{n+q}^{s\cdot s''} - \frac{\epsilon_{p,q}^{s',s''}}{\lambda^p} u_{n-p}^{s\cdot s',*} u_{n+q-p}^{s\cdot s'\cdot s''} + \frac{\xi_{p,q}^{s',s''}}{\lambda^q} u_{n-q}^{s\cdot s''} u_{n+p-q}^{s\cdot s'\cdot s''} \right), \tag{A8}$$

where λ and k_0 are free parameters and $D_n \equiv \nu k_n^2$. The helical signs of the interacting modes depend on the specific $\{s',s''\}$ set, here written compactly by introducing effective signs built on products of s, s', and s'', e.g., $s \cdot s'$. The triad shape weight $G_{p,q}$, submodel weight $g_{p,q}^{s',s''}$, and modal interaction coefficients $\epsilon_{p,q}^{s',s''}$ and $\xi_{p,q}^{s',s''}$ are given by

$$G_{p,q}(\lambda) = 1/8 \, (2\lambda^{-2q} + 2\lambda^{-2p} + 2 - \lambda^{-2(p+q)} - \lambda^{2(p-q)}$$
$$- \lambda^{2(q-p)})^{1/2}, \tag{A9}$$

$$g_{p,q}^{s',s''}(\lambda) = -s's''(1 + s'\lambda^p - s''\lambda^q)(s'\lambda^p - s''\lambda^q), \tag{A10}$$

$$\epsilon_{p,q}^{s',s''}(\lambda) = \frac{1 - s''\lambda^q}{\lambda^p - s's''\lambda^q}, \tag{A11}$$

$$\xi_{p,q}^{s',s''}(\lambda) = -s''\left(1 - s'\epsilon_{p,q}^{s',s''}\right). \tag{A12}$$

APPENDIX B: INTERACTION WEIGHTS

The functional forms of the three interaction coefficients $g_{p,q}^{s',s''}, \epsilon_{p,q}^{s',s''}$, and $\xi_{p,q}^{s',s''}$ in their local limit are addressed in Sec. II. Figure 7 shows plots of the remaining triad shape weight $G_{p,q}$, ranging from the limit of local interactions ($\{p,q\} = \{1,2\}$) to nonlocal ($q = p + 1$, $p \gg 1$) [Fig. 7(a)] and reduced nonlocal ($q = p + i$, where $1 \leqslant i \leqslant 3$) interactions [Fig. 7(b)]. Three important results are noticed here. First, the K41 assumption of local interactions being dominant is supported by $G_{p,q}$. Second, $G_{p,q}$ is proportional to the area of the triangle formed by $\{k,k',k''\}$, thereby automatically ensuring that the triangle inequality is fulfilled by $G_{p,q} = 0$ if $k_n + k_{n+p} < k_{n+q}$. Consequently, interactions are well defined only for

$1 \leqslant \lambda \leqslant \varphi$, where φ is the golden ratio. Third, reducing the nonlocalness of interactions by tending towards coupling three different scales weighs less compared to interactions involving two comparable scales [$p \sim q$ in Fig. 7(b)].

APPENDIX C: INVARIANTS

In the helical basis the energy and helicity take the simple form $E = \sum_{n=0}^{N}(|u_n^+|^2 + |u_n^-|^2)$ and $H = \sum_{n=0}^{N} k_n(|u_n^+|^2 - |u_n^-|^2)$, where $n = 0$ and $n = N$ are the first and last shells [1]. Here, however, we consider generalized quadratic invariants as introduced in Sec. I. Consider therefore the generalized energy-like and helicity-like quantities

$$E^{(\alpha)} = \sum_{n=0}^{N} k_n^{\alpha}(|u_n^+|^2 + |u_n^-|^2), \tag{C1}$$

$$H^{(\beta)} = \sum_{n=0}^{N} k_n^{\beta}(|u_n^+|^2 - |u_n^-|^2), \tag{C2}$$

where α and β are some yet to be determined exponents. In this notation energy is given by $\alpha = 0$ and helicity by $\beta = 1$.

It turns out that each of the four submodels, here defined as the four contributions from $\sum_{s',s''}$ in (A8) (Sec. II), inviscidly conserve the energy and helicity separately for every triad shape ($\{p,q,\lambda\}$ set). Taking the time derivative of (C1) using (A8) and telescoping sums by assuming a finite wave set (i.e., $u_n^s = 0$ for $n < 0$ and $n > N$), one finds the nonlinear (N.L.) rate of change of $E^{(\alpha)}$ is given by the long but straightforward
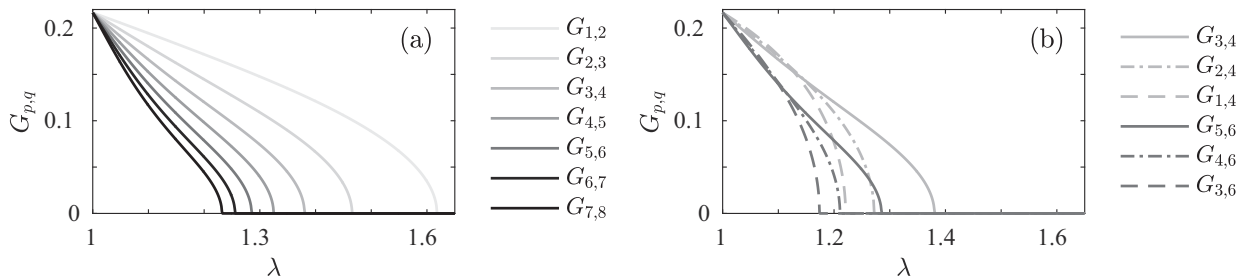
FIG. 7. Triad interaction weight $G_{p,q}$ as a function of the triad geometry for (a) local ($\{p,q\} = \{1,2\}$) to nonlocal ($q = p + 1$, $p \gg 1$) triads and (b) reduced nonlocal ($q = p + i$ where $1 \leqslant i \leqslant 3$) triads.

calculation

$$d_t|_{\text{N.L.}} E^{(\alpha)} = \sum_{n=0}^{N} k_n^{\alpha}(u_n^{+,*} d_t u_n^+ + u_n^{-,*} d_t u_n^-) + \text{c.c.}$$

$$= \sum_{\substack{p,\,q \\ 0<p<q \\ k_n+k_{n+p} \geqslant k_{n+q}}} G_{p,q} \sum_{s',s''} g_{p,q}^{s',s''} \sum_{n=q}^{N} k_{n-q}^{\alpha+1} \big[\big(u_{n-q}^{+,*} u_{n-q+p}^{s',*} u_n^{s''} - u_{n-q}^{-,*} u_{n-q+p}^{-s',*} u_n^{-s''} \big)$$

$$- (\lambda^{\alpha})^p \epsilon_{p,q}^{s',s''} \big(u_{n-q}^{s',*} u_{n-q+p}^{+,*} u_n^{s's''} - u_{n-q}^{-s',*} u_{n-q+p}^{-,*} u_n^{-s's''} \big) + (\lambda^{\alpha})^q \xi_{p,q}^{s',s''} \big(u_{n-q}^{s'',*} u_{n-q+p}^{s's'',*} u_n^+ - u_{n-q}^{-s'',*} u_{n-q+p}^{-s's'',*} u_n^- \big) \big] + \text{c.c.}$$

$$\text{(C3)}$$

From here it is noted that the second and third velocity triple-product differences are equal to the first times s' and s'', respectively, that is,

$$u_{n-q}^{s',*} u_{n-q+p}^{+,*} u_n^{s's''} - u_{n-q}^{-s',*} u_{n-q+p}^{-,*} u_n^{-s's''}$$
$$= s' \big(u_{n-q}^{+,*} u_{n-q+p}^{s',*} u_n^{s''} - u_{n-q}^{-,*} u_{n-q+p}^{-s',*} u_n^{-s''} \big) \qquad \text{(C4)}$$

$$u_{n-q}^{s'',*} u_{n-q+p}^{s's'',*} u_n^+ - u_{n-q}^{-s'',*} u_{n-q+p}^{-s's'',*} u_n^-$$
$$= s'' \big(u_{n-q}^{+,*} u_{n-q+p}^{s',*} u_n^{s''} - u_{n-q}^{-,*} u_{n-q+p}^{-s',*} u_n^{-s''} \big), \qquad \text{(C5)}$$

thus allowing the triple-product differences to be moved outside the square brackets. A similar calculation may be done for $H^{(\beta)}$, yielding a positive sign between the velocity triple products, implying that all three triple-product sums are similar. Tidying up by defining correlators as

$$\Delta_{n,p,q}^{\pm,s',s''} \equiv 2k_{n-q} \, \text{Re} \left[u_{n-q}^{+,*} u_{n-q+p}^{s',*} u_n^{s''} \pm u_{n-q}^{-,*} u_{n-q+p}^{-s',*} u_n^{-s''} \right] \qquad \text{(C6)}$$

the generalized energy and helicity equations become

$$d_t|_{\text{N.L.}} E^{(\alpha)} = \sum_{\substack{p,\,q \\ 0<p<q \\ k_n+k_{n+p} \geqslant k_{n+q}}} G_{p,q} \sum_{s',s''} g_{p,q}^{s',s''} \mathscr{E}_{p,q}^{s',s''} \sum_{n=q}^{N} k_{n-q}^{\alpha} \Delta_{n,p,q}^{-,s',s''}$$

$$\text{(C7)}$$

$$d_t|_{\text{N.L.}} H^{(\beta)} = \sum_{\substack{p,\,q \\ 0<p<q \\ k_n+k_{n+p} \geqslant k_{n+q}}} G_{p,q} \sum_{s',s''} g_{p,q}^{s',s''} \mathscr{H}_{p,q}^{s',s''} \sum_{n=q}^{N} k_{n-q}^{\beta} \Delta_{n,p,q}^{+,s',s''}$$

$$\text{(C8)}$$

where the three correlator prefactors in (C3) (and correspondingly for the helicity) have been grouped together

by

$$\mathscr{E}_{p,q}^{s',s''}(\lambda^{\alpha}) = 1 - s'(\lambda^{\alpha})^p \epsilon_{p,q}^{s',s''} + s''(\lambda^{\alpha})^q \xi_{p,q}^{s',s''}, \qquad \text{(C9)}$$

$$\mathscr{H}_{p,q}^{s',s''}(\lambda^{\beta}) = 1 - (\lambda^{\beta})^p \epsilon_{p,q}^{s',s''} + (\lambda^{\beta})^q \xi_{p,q}^{s',s''}. \qquad \text{(C10)}$$

Equations (C9) and (C10) are in fact equal to the generalized conservation constraints, (6) and (7), imposed by the NSE by noting that $\{k,k',k''\} = \{k_n, k_{n+p}, k_{n+q}\}$.

The conservation of $E^{(\alpha)}$ and $H^{(\beta)}$ thus requires $\mathscr{E}_{p,q}^{s',s''}(\lambda^{\alpha}) = 0$ and $\mathscr{H}_{p,q}^{s',s''}(\lambda^{\beta}) = 0$. Plugging $\alpha = 0$ into $\mathscr{E}_{p,q}^{s',s''}(\lambda^{\alpha})$ one finds that the energy is always conserved independently of the triad shape ($\{\lambda, p, q\}$) and submodel ($\{s', s''\}$). Other solutions to $\mathscr{E}_{p,q}^{s',s''}(\lambda^{\alpha}) = 0$, however, depend on the specific submodel and triad shape resolved. Since these solutions are not shared across triad shapes or submodels, the remaining invariants can be considered triad shape- and submodel-specific invariants, or *pseudoenergy invariants*, because they are broken when mixing triad shapes and/or submodels, just as in the NSE. In a similar fashion, each submodel inviscidly conserves the helicity ($\beta = 1$) separately for every triad shape since $\mathscr{H}_{p,q}^{s',s''} = 0$ by substituting (A11) and (A12) in. The remaining helicity-like invariants behave similarly to the energy-like invariants and are thus denoted *pseudohelicity invariants*.

Note that because of the polynomial structure of (C9) and (C10), any triad shape configuration given by $\{\lambda, p, q\}$ will have $q - 1$ pseudoenergy invariants and $q - 1$ pseudohelicity invariants.

APPENDIX D: SPECTRAL FLUXES

Nonlinear spectral fluxes of $E^{(\alpha)}$ and $H^{(\beta)}$ through the nth shell are given as the transfers from all wave numbers less than k_n to wave numbers greater than k_n, that is, $\Pi_n^{E^{(\alpha)}} = d_t|_{\text{N.L.}} \sum_{m=0}^{n} k_m^{\alpha}(|u_m^+|^2 + |u_m^-|^2)$ and $\Pi_n^{H^{(\beta)}} = d_t|_{\text{N.L.}} \sum_{m=0}^{n} k_m^{\beta}(|u_m^+|^2 - |u_m^-|^2)$. Following the calculations through, one finds that (C3) becomes (breaking the sum at n instead of N)

$$\Pi_n^{E^{(\alpha)}} = \sum_{\substack{p,\,q \\ 0<p<q \\ k_n+k_{n+p} \geqslant k_{n+q}}} G_{p,q} \sum_{s',s''} g_{p,q}^{s',s''} \left[\mathscr{E}_{p,q}^{s',s''} \sum_{m=q}^{n} k_{m-q}^{\alpha} \Delta_{m,p,q}^{-,s',s''} + \sum_{m=n+1}^{n+q} k_{m-q}^{\alpha} \Delta_{m,p,q}^{-,s',s''} - s' \epsilon_{p,q}^{s',s''} \sum_{m=n+1}^{n+q-p} k_{m-q+p}^{\alpha} \Delta_{m,p,q}^{-,s',s''} \right], \qquad \text{(D1)}$$

where summation over the shared range $q \leqslant m \leqslant n$ has been grouped together in the first term. This term, however, vanishes since $\mathscr{E}_{p,q}^{s',s''}(\lambda^{\alpha}) = 0$ for $E^{(\alpha)}$ to be an invariant. Going through similar calculations for $\Pi_n^{H^{(\beta)}}$ one finally finds that the spectral

fluxes are given by

$$\Pi_n^{E^{(\alpha)}} = \sum_{\substack{p,\,q \\ 0<p<q \\ k_n+k_{n+p}\geqslant k_{n+q}}} G_{p,q} \sum_{s',s''} g_{p,q}^{s',s''} \left[\sum_{m=n+1}^{n+q} k_{m-q}^{\alpha} \Delta_{m,p,q}^{-,s',s''} - s'\epsilon_{p,q}^{s',s''} \sum_{m=n+1}^{n+q-p} k_{m-q+p}^{\alpha} \Delta_{m,p,q}^{-,s',s''} \right], \tag{D2}$$

$$\Pi_n^{H^{(\beta)}} = \sum_{\substack{p,\,q \\ 0<p<q \\ k_n+k_{n+p}\geqslant k_{n+q}}} G_{p,q} \sum_{s',s''} g_{p,q}^{s',s''} \left[\sum_{m=n+1}^{n+q} k_{m-q}^{\beta} \Delta_{m,p,q}^{+,s',s''} - \epsilon_{p,q}^{s',s''} \sum_{m=n+1}^{n+q-p} k_{m-q+p}^{\beta} \Delta_{m,p,q}^{+,s',s''} \right]. \tag{D3}$$

[1] F. Waleffe, The nature of triad interactions in homogeneous turbulence, Phys. Fluids A **4**, 350 (1992).

[2] L. Biferale, S. Musacchio, and F. Toschi, Inverse Energy Cascade in Three-Dimensional Isotropic Turbulence, Phys. Rev. Lett. **108**, 164501 (2012).

[3] E. B. Gledzer, System of hydrodynamic type admitting two quadratic integrals of motion, Soviet Physics Doklady **18**, 216 (1973).

[4] V. S. L'vov, E. Podivilov, A. Pomyalov, I. Procaccia, and D. Vandembroucq, Improved shell model of turbulence, Phys. Rev. E **58**, 1811 (1998).

[5] P. D. Ditlevsen, Symmetries, invariants, and cascades in a shell model of turbulence, Phys. Rev. E **62**, 484 (2000).

[6] L. Biferale and R. M. Kerr, Role of inviscid invariants in shell models of turbulence, Phys. Rev. E **52**, 6113 (1995).

[7] R. Benzi, L. Biferale, R. M. Kerr, and E. Trovatore, Helical shell models for three-dimensional turbulence, Phys. Rev. E **53**, 3541 (1996).

[8] L. Biferale, D. Pierotti, and F. Toschi, Helicity transfer in turbulent models, Phys. Rev. E **57**, R2515 (1998).

[9] L. Biferale, D. Pierotti, and F. Toschi, Helicity advection in turbulent models, J. Phys. IV France **08**, Pr6-131 (1998).

[10] M. De Pietro, L. Biferale, and A. A. Mailybaev, Inverse energy cascade in nonlocal helical shell models of turbulence, Phys. Rev. E **92**, 043021 (2015).

[11] A. Brissaud, U. Frisch, J. Leorat, M. Lesieur, and A. Mazure, Helicity cascades in fully developed isotropic turbulence, Phys. Fluids (1958–1988) **16**, 1366 (1973).

[12] P. D. Ditlevsen and I. A. Mogensen, Cascades and statistical equilibrium in shell models of turbulence, Phys. Rev. E **53**, 4785 (1996).

[13] R. Kraichnan and D. Montgomery, Two-dimensional turbulence, Rep. Prog. Phys. **43**, 547 (1980).

[14] T. Gilbert, V. S. L'vov, A. Pomyalov, and I. Procaccia, Inverse Cascade Regime in Shell Models of Two-Dimensional Turbulence, Phys. Rev. Lett. **89**, 074501 (2002).